

## Effect Mechanisms of Hygrothermal Environments on Failure of Single-Lap and Double-Lap CFRP-Aluminum Bolted Joints

Meijuan Shan<sup>1, 2</sup>, Libin Zhao<sup>2, \*</sup>, Wei Huang<sup>3</sup>, Fengrui Liu<sup>2</sup> and Jianyu Zhang<sup>4, \*</sup>

**Abstract:** The high demands for load-carrying capability and structural efficiency of composite-metal bolted joints trigger in-depth investigations on failure mechanisms of the joints in hygrothermal environments. However, few studies have been presented to exhaustively reveal hygrothermal effects on the failure of CFRP-metal bolted joints, which differ from CFRP-CFRP or metal-metal bolted joints because of the remarkably different material properties of CFRPs and metals. In this paper, hygrothermal effects on tensile failures of single-lap and double-lap CFRP-aluminum bolted joints were experimentally and numerically investigated. A novel numerical model, in which a hygrothermal-included progressive damage model of composites was established and elastic-plastic models of metals were built, was proposed to predict the failures of the CFRP-metal bolted joints in hygrothermal environments and validated by corresponding experiments. Different failure mechanisms of single-lap and double-lap CFRP-aluminum bolted joints, under 23°C/Dry and 70°C/Wet conditions, were revealed, respectively. It follows that both the collapse failures of the single-lap and double-lap bolted joints were dominated by the bearing failure of the CFRP hole laminate in the two conditions, indicating that the hygrothermal environment did not change the macro failure modes of the joints. However, the hygrothermal environment considerably shortened the damage propagation processes and reduced the strength of the joints. Besides, the hygrothermal environment weakened the load-transfer capability of the single-lap joint more severely than the double-lap joint because it aggravated the secondary bending effects of the single-lap joint obviously.

**Keywords:** CFRP-metal hybrid structure, bolted joint, hygrothermal environment, effect mechanism, numerical model.

---

<sup>1</sup> Department of Mechanics, School of Civil Engineering, Beijing Jiaotong University, Beijing, 100044, China.

<sup>2</sup> School of Astronautics, Beihang University, Beijing, 100191, China.

<sup>3</sup> Hubei Aerospace Flight Vehicle Institute, Wuhan, 430040, China.

<sup>4</sup> College of Aerospace Engineering, Chongqing University, Chongqing, 400044, China.

\* Corresponding Author: Libin Zhao. Email: lbzhao@buaa.edu.cn; Jianyu Zhang. Email: jyzhang@cqu.edu.cn.

Received: 17 November 2019; Accepted: 13 January 2020.

## 1 Introduction

Carbon fiber reinforced polymers (CFRPs) have been increasingly used in highly-loaded structures of advanced aircrafts, marine equipment and automobiles for the purpose of improving structural efficiencies as well as enhancing overall performances, due to the high specific stiffness/strength, superior fatigue performance, etc. Despite their popularity, CFRPs cannot completely replace the metal materials (such as aluminum, titanium, steel, etc.) because of the specific requirements of highly-loaded structures. For this reason, highly-loaded structures are usually hybrid structures composed of CFRPs and metals, and therefore the joining between these two dissimilar materials is essential in the design of the highly-loaded structures [Banea, Rosioara, Carbas et al. (2018); Graham, Rezai, Baker et al. (2014); Li, Zhang, Cheng et al. (2019); Pitta, Carles, Roure et al. (2018); Pramanik, Basak, Dong et al. (2017); Tang and Liu (2018); Zhang, Zhang, Fan et al. (2019)]. Among the various joining methods, mechanically fastened joints (bolt, rivet, pin, screw, etc.) are mainly used by virtue of the high reliability and easy-to-assembly/disassembly/maintenance, etc. [Mangalgi (2013); McCarthy (2001); Meram and Can (2019)].

As we all know, the accurate failure predictions of the fastened joints are of great importance for the efficient design of the highly-loaded structures because the joints are weak points of the structures. Although the failure prediction methods and failure mechanisms of CFRP-CFRP or metal-metal fastened joints have been thoroughly investigated during the last decades [Camanho and Matthews (1997); Coelho and Mottram (2015); Egan, McCarthy, McCarthy et al. (2013); Giannopoulos, Dawes, Kourousis et al. (2017); Li, Gu and Zhao (2017); Liu, Lu, Zhao et al. (2018); Tajeuna, Légeron, Labossière et al. (2015); Thoppul, Finegan and Gibson (2009); Tian, Xiong and Liu (2015); Tüzemen, Salame and Avc (2017); Zhao, Shan, Liu et al. (2017)], the remarkable difference in mechanical properties of CFRP and metal materials causes new problems that need to be solved with regard to the failure analyses of CFRP-metal hybrid fastened joints. Naarayan et al. [Naarayan, Kumar and Chandra (2009)] compared rivet load distributions of CFRP-metal multi-rivet joints with those of metal-metal and CFRP-CFRP joints, and suggested that metal plates of the CFRP-metal hybrid joints considerably affect redistributions of rivet loads, which further influences the failure behaviour of the joints. Besides, CFRP-aluminum single-lap and double-lap bolted joints as proposed for use in a wing-box were selected as benchmark structures in BOJCAS, and the failures of the joints were evaluated by finite element (FE) models and experiments [Ekh, Schön and Melin (2005, 2006); Ekh, Schön and Zenkert (2013); Ekh and Schön (2008); McCarthy (2001); Riccio and Marciano (2005); Riccio (2005)]. Ahmad et al. predicted the failures of single-lap and double-lap CFRP-steel bolted joints under quasi-static tensile loadings using XFEM [Ahmad, Crocombe and Smith (2013, 2014)]. Liu et al. [Liu, Zhang, Chen et al. (2015); Liu (2014)] and Yang et al. [Yang, Yue, Geng et al. (2017)] also predicted the quasi-static tensile properties of CFRP-metal single-lap bolted joints via FE models that considered the progressive damage property of composites and the elastic-plasticity of metals.

Lately, failures of CFRP-metal fastened joints under tensile dynamic and fatigue loadings were researched by experiments [Jiang, Li, Zhang et al. (2017); Rao, Kang, Huff et al. (2018); VanderKlok, Dutta and Tekalur (2013); Zuo, Cao, Cao et al. (2018)]. Askri et al. [Askri, Bois, Wargnier et al. (2018)] analyzed the probabilistic failure of CFRP-metal fastened joints.

Further, the failure behaviour of CFRP-metal fastened joints becomes more complex under severe environments (such as elevated temperature, high humidity and corrosion, etc.) because of the remarkable difference in material properties of CFRPs and metals. Several studies have investigated thermal effects on the failure behaviour of CFRP-metal bolted joints [Abdus, Cheng, Huang et al. (2019); Caccese, Berube, Fernandez et al. (2009); Coman and Constantinescu (2019); Comer, Dhôte, Stanley et al. (2012); Gay, Lefebvre, Bergamo et al. (2016); Horn and Schmitt (1993); Kapidzic, Nilsson and Ansell (2014); Kapidzic, Ansell, Schön et al. (2015a, 2015b); Kapidzic, Ansell, Schön et al. (2016); Kradinov, Barut, Madenci et al. (2001); Nichols, Trickey, Seaver et al. (2007)]. Horn et al. [Horn and Schmitt (1993)], Nichols et al. [Nichols, Trickey, Seaver et al. (2007)] and Caccese et al. [Caccese, Berube, Fernandez et al. (2009)] revealed thermal effects on clamp-up force relaxations of FRP-metal single-lap bolted joints, which further reduced failure loads of the joints. Kradinov et al. [Kradinov, Barut, Madenci et al. (2001)] focused on thermal effects on bolt load distributions of CFRP-aluminum single-lap and double-lap multi-bolt joints. Kapidzic et al. [Kapidzic, Nilsson and Ansell (2014)] analyzed bolt load distributions of complicated CFRP-aluminum multi-bolt joints used in aircraft primary structures under thermal-mechanical loads, and concluded that the considerable fastener forces caused by the elevated temperature should be considered in the design of the hybrid bolted joints. They also investigated thermal effects on quasi-static and fatigue bearing failures of a CFRP-aluminum two-bolt joint, and suggested that the thermally-induced load coupled to the mechanical load had a negligible effect on the bearing strength of the joint, whereas affected the damage accumulation process and final failure pattern of the joint [Kapidzic, Ansell, Schön et al. (2015a, 2015b, 2016)]. Comer et al. [Comer, Dhôte, Stanley et al. (2012)] and Gay et al. [Gay, Lefebvre, Bergamo et al. (2016)] evaluated thermal effects on fatigue stiffness and strength of FRP-aluminum fastened joints. These researches showed that the elevated temperature considerably affected the failure behaviour of the CFRP-metal hybrid bolted joints.

The hygrothermal environment (elevated temperature and moisture absorption), which is common in practical applications, is deemed to be a more severe environmental factor that significantly affects the failure behaviour of the CFRP-metal bolted joints [Mangalgiri (2013)]. The elevated temperature coupled with moisture absorption greatly weakens the matrix as well as the interface of matrix and fiber, which further reduces material properties of CFRPs. Besides, the anisotropic hygrothermal expansion characteristics of CFRPs cause complicated hygrothermal stresses in the multidirectional CFRP laminate of the joints. The hygrothermal environment also changes contact relationships between CFRP and metal components of the joints. Accordingly, the

hygrothermal environment has multiscale and complicated influences on failure mechanisms of the CFRP-metal hybrid bolted joints. However, how the hygrothermal environment affects the failure behaviour of the CFRP-metal bolted joints remains largely unexplored.

This paper aims to fully reveal effects of the hygrothermal environment on tensile failures of single-lap and double-lap CFRP-aluminum hybrid bolted joints. The sub-objectives are: 1) to develop a novel numerical model that can accurately predict the failure of the joints in hygrothermal environments; 2) to distinguish the different failure mechanisms of the joints in Room Temperature 23°C/Dry (RTD) and Elevated Temperature 70°C/Wet (ETW) conditions; 3) to elaborate the different effect mechanisms of the hygrothermal environment on the failures of the single-lap and double-lap joints. To achieve these purposes, this paper is organized as follows. Section 2 presented specimen design scheme and experimental procedure; Section 3 proposed a numerical model and validated it by experiments; Section 4 analyzed the hygrothermal effects on failure mechanisms of the joints based on experiments; Section 5 conducted thorough analyses of the hygrothermal effect based on the numerical results, followed by conclusions in Section 6.

## 2 Specimen design scheme and experimental procedure

### 2.1 Specimen design scheme

As discussed above, single-lap and double-lap joints are regarded as the benchmarks in previous researches. Therefore, both single-lap and double-lap CFRP-aluminum single-bolt joints, as listed in [Tab. 1](#), are designed to determine effects of the hygrothermal environment on failure mechanisms of the joints as well as to ascertain influences of the joining type on failure mechanisms of the joints in hygrothermal environments. Two environmental conditions including Room Temperature 23°C/Dry (RTD) and Elevated Temperature 70°C/Wet (ETW) are considered, and the numbers of the specimens are presented in [Tab. 1](#).

As shown in [Fig. 1](#), CFRP laminates of the joints are fabricated from a unidirectional prepreg with a quasi-isotropic stacking sequence of  $[45/0/-45/90]_{2s}$ . The unidirectional prepreg is made of T800 carbon fiber and CYCOM<sup>®</sup> X850 epoxy resin. The aluminum

**Table 1:** Scheme design of the CFRP-aluminum hybrid bolted joints

Configuration	Group No.	Environmental condition	Number
Single-lap, single-bolt joint	1	Room Temperature 23°C/Dry (RTD)	3
	2	Elevated Temperature 70°C/Wet (ETW)	4
Double-lap, single-bolt joint	3	Room Temperature 23°C/Dry (RTD)	3
	4	Elevated Temperature 70°C/Wet (ETW)	4

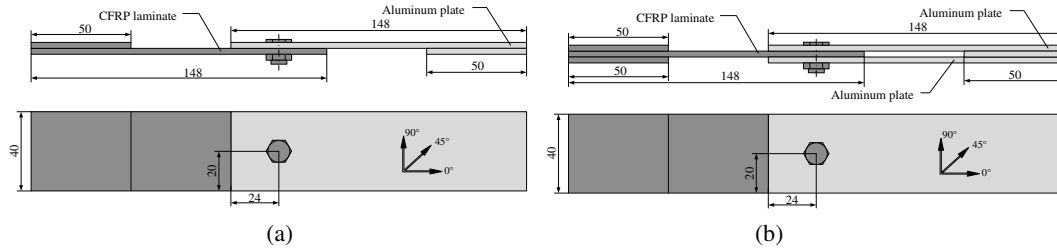


**Figure 1:** Configurations and dimensions of the CFRP-aluminum bolted joints (Unit: mm). (a) Single-lap joint (b) Double-lap joint

plates of the joints are made of 7050-T7451 aluminum alloy. The fastener system consists of a hexagon bolt and a hexagon nut, both of which are made of Ti-6Al-4V titanium alloy. The fastener is finely manufactured and processed referred to the aviation industry standard HB 8022. A tightening torque of 2.1 N·m is applied on the fastener.

Besides, the dimensions of the joints are also depicted in Fig. 1. The dimensions of the CFRP laminate are determined according to the standard ASTM D5961 [ASTM D5961M-13 (2013)]. The nominal diameter of the hole  $D$  in the laminate is 8 mm, thus the width to diameter ratio  $W/D=5$  and the edge distance ratio  $E/D=3$ . The nominal thickness of the unidirectional prepreg is 0.185 mm and therefore the thickness of the CFRP laminates is 2.96 mm. The dimensions of the aluminum plate are the same as those of the CFRP laminate. The nominal diameter of the bolt shank is 8 mm with the upper and lower variations of tolerance being -0.013 mm and -0.049 mm. The length of the bolt shank is 18 mm.

The mechanical properties of the unidirectional prepreg in the RTD condition are presented in Tab. 2, in which the intralaminar properties are provided by the manufacturer, and the interlaminar properties are determined by the transversely isotropic assumption except that  $v_{23}^0 = v_{12}^0(1 - v_{12}^0 E_{22}^0/E_{11}^0)/(1 - v_{12}^0)$  and  $S_{23}^0 = Y_C^0/2 \tan(53^\circ)$ .

## 2.2 Experimental procedure

The procedures for the static tensile tests of the hybrid bolted joints in the RTD and ETW conditions are depicted in Fig. 2. First is the accelerated moisture absorption test according to ASTM D5229M-14 [ASTM D5229M-14 (2014)], during which eight CFRP laminate specimens are immersed into a 70°C thermostat water bath and the weight of the specimens is regularly measured by an electronic analytical balance FA2004 with the precision of 0.1 mg. When the mass increment of two consecutive measurements is less than 0.02%, the specimen achieves the effective moisture equilibrium [ASTM D5229M-14 (2014)]. After about 800 hours, the moisture absorption is stopped with a balanced moisture content of 0.62%. Subsequently, the eight CFRP laminate specimens in wet state and six CFRP laminate specimens in dry state are assembled with aluminum plates using a tightening torque wrench, to obtain seven single-lap and seven double-lap joint specimens. After that, quasi-static tensile tests of the joint specimens are conducted by the Instron-8803 testing machine. An environment chamber is used to control the

**Table 2:** Material properties of the T800 carbon/epoxy composites in the RTD condition

Items	Values
Longitudinal elastic modulus $E_{11}^0$ (GPa)	163.5
Transverse elastic modulus $E_{22}^0 = E_{33}^{0*}$ (GPa)	9.00
Shear modulus $G_{12}^0 = G_{13}^{0*}$ (GPa)	4.14
Shear modulus $G_{23}^{0*}$ (GPa)	3.08
Poisson's ratio $\nu_{12}^0 = \nu_{13}^{0*}$	0.32
Poisson's ratio $\nu_{23}^{0*}$	0.46
Longitudinal tensile strength $X_T^0$ (MPa)	2992
Longitudinal compressive strength $X_C^0$ (MPa)	1183
Transverse tensile strength $Y_T^0 = Z_T^{0*}$ (MPa)	70.6
Transverse compressive strength $Y_C^0 = Z_C^{0*}$ (MPa)	278
Shear strength $S_{12}^0 = S_{13}^{0*}$ (MPa)	172
Shear strength $S_{23}^{0*}$ (MPa)	105

temperature at 70°C. A continuously increasing tensile load is applied to the specimens at a loading rate of 1 mm/min until the collapse failure occurs. The load-displacement curves as well as the ultimate failure loads of the joint specimens are automatically recorded by the testing programs.

### 3 Novel numerical model involving hygrothermal effects

The composite-metal bolted joint includes three components, namely the composite laminate, the metal plate and the metal bolt. The competing failure occurs among these components when the joint is subjected to external loads, and the failure of the weakest one causes the collapse failure of the joint. Therefore, the accurate description of mechanical behaviour of the three components is crucial for predicting the failure of the hybrid bolted joints. In this paper, a progressive damage model (PDM) that included hygrothermal effects was proposed to evaluate the failure of the CFRP laminate, and elastic-plastic models were established to describe material properties of the aluminum plate and the titanium bolt. Both of them were employed in the FE models of the single-lap and double-lap joints to predict the collapse failures of the joints. The proposed numerical model was validated by the experimental results.

#### 3.1 Hygrothermal-included PDM of composites

To determine material properties of the T800 carbon/epoxy unidirectional prepreg, which are significantly influenced by the hygrothermal environment, a unified model proposed in our previous research [Shan, Zhao, Hong et al. (2018)] is used. The equations are

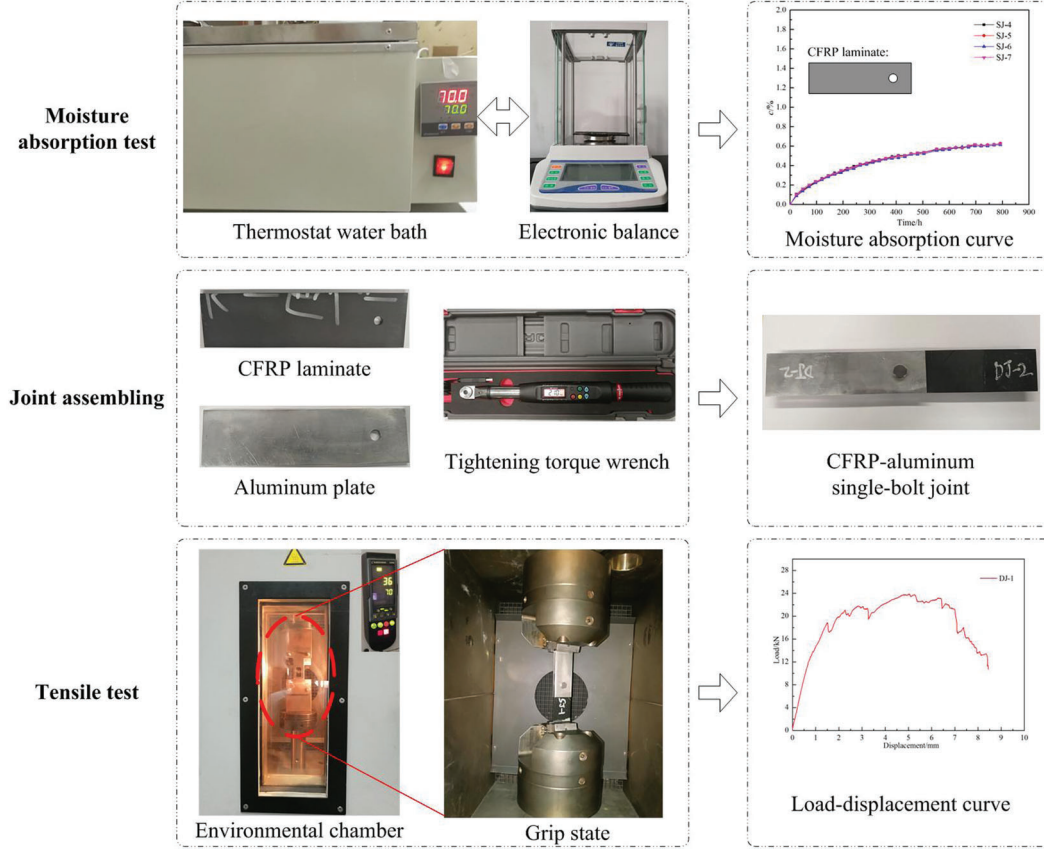


**Figure 2:** Procedures for the tensile tests of the CFRP-aluminum bolted joints in hygrothermal environments

$$\begin{aligned} \frac{E_{11}^{\text{hyg}}}{E_{11}^0} &= (T^*)^a, \quad \frac{E_{22}^{\text{hyg}}}{E_{22}^0} = (T^*)^b, \quad \frac{G_{12}^{\text{hyg}}}{G_{12}^0} = (T^*)^c, \quad \frac{\nu_{12}^{\text{hyg}}}{\nu_{12}^0} = 1, \\ \frac{X_T^{\text{hyg}}}{X_T^0} &= (T^*)^d, \quad \frac{X_C^{\text{hyg}}}{X_C^0} = (T^*)^e, \quad \frac{Y_T^{\text{hyg}}}{Y_T^0} = (T^*)^f, \quad \frac{Y_C^{\text{hyg}}}{Y_C^0} = (T^*)^g, \quad \frac{S_{12}^{\text{hyg}}}{S_{12}^0} = (T^*)^h \end{aligned} \quad (1)$$

where the nondimensional temperature  $T^* = (T_g - T) / (T_g^0 - T_0)$ .  $T_g$  and  $T_g^0$  denote the glass transition temperatures of the composites at wet and dry states.  $T$  and  $T_0$  represent the test temperature and room temperature, respectively.  $a$ ,  $b$ ,  $c$ ,  $d$ ,  $e$ ,  $f$ ,  $g$  and  $h$  are the fitted exponent parameters. More details of the unified model can be found in Shan et al. [Shan, Zhao, Hong et al. (2018)].

Besides, the hygrothermal environment causes additional strains in the composites and changes the stress-strain relationship, which is expressed as

$$\boldsymbol{\sigma} = \mathbf{C}(\boldsymbol{\varepsilon} - \boldsymbol{\alpha}\Delta T - \boldsymbol{\beta}C), \quad (2)$$

where  $\boldsymbol{\sigma}$  and  $\boldsymbol{\varepsilon}$  denote the stresses and strains of the composites in the principal material coordinate system, respectively. The stiffness matrix  $\mathbf{C}$  is the function of material properties.  $\boldsymbol{\alpha}$  and  $\boldsymbol{\beta}$  are the coefficients of the thermal expansion and moisture expansion, respectively. The temperature variation  $\Delta T = T - T_0$  and the moisture content  $C = (W - W_0)/W_0 \times 100\%$ , where  $W$  and  $W_0$  are the weight of the structure after moisture and the initial weight, respectively.

As discussed above, the hygrothermal environment changes the stresses of the multidirectional composite laminates under the mechanical load. With the increase of the mechanical load, the damage happens in composites. The hygrothermal environment also influences the damage properties of the composites. Thus, a Hashin-type failure criterion [Tserpes, Labeas, Papanikos et al. (2002)] and a micromechanics-based material degradation model [Zhang, Zhou, Chen et al. (2016)] are modified to predict the progressive damage process of the unidirectional composites in hygrothermal environments, as presented in Tab. 3. In the modified Hashin-type failure criterion, the ultimate strengths varying with the hygrothermal environment are used to replace the constant ultimate strengths in the traditional criterion. Once the failure of the composites is detected by the failure criterion, the stiffness of the composites degenerates according to the material degradation rules in Tab. 3, where the degradation factors  $d_i^{hyg}$  ( $i = ft, fc, mt, mc, dt, dc, fm1$  or  $fm2$ ) are dependent on the hygrothermal environment and calculated by Eqs. (3) and (4).

$$\begin{aligned} d_{ft}^{hyg} &= (T^*)^{j-a} d_{ft}^0, d_{fc}^{hyg} \approx (T^*)^{b-a} d_{fc}^0 \\ d_{mt}^{hyg} &= d_{dt}^{hyg} = 0, d_{mc}^{hyg} = d_{dc}^{hyg} \approx 0 \\ d_{fm1}^{hyg} &= (T^*)^{j-c} d_{fm1}^0, d_{fm2}^{hyg} = (T^*)^{j-c} d_{fm2}^0 \end{aligned} \quad (3)$$

$$\begin{aligned} d_{ft}^0 &= \frac{V_m E_m^0}{E_{11}^0}, d_{fc}^0 \approx \frac{E_{22}^0}{E_{11}^0} \\ d_{mt}^0 &= d_{dt}^0 = 0, d_{mc}^0 = d_{dc}^0 \approx 0 \\ d_{fm1}^0 &= \left( \frac{1 - \sqrt{V_f}}{1 - \sqrt{V_f} + V_f} \right) \frac{G_m^0}{G_{12}^0}, d_{fm2}^0 = \left( \frac{1 - \sqrt{V_f}}{1 - \sqrt{V_f} + V_f} \right) \frac{G_m^0}{G_{23}^0} \end{aligned} \quad (4)$$

The parameters  $T^*$ ,  $a$ ,  $b$ ,  $c$  in Eq. (3) is the same as those in Eq. (1), and the parameter  $j$  is the exponent when the nondimensional temperature  $T^*$  is used to fit the elastic modulus  $E_m$  and the shear modulus  $G_m$  of the matrix as the functions of the hygrothermal environment.  $d_i^0$  ( $i = ft, fc, mt, mc, dt, dc, fm1$  or  $fm2$ ) are the degradation factors in the standard laboratory environment.  $V_m$  and  $V_f$  are the volume fractions of the fiber and matrix, respectively.

**Table 3:** Modified Hashin-type failure criterion and micromechanics-based material degradation model

Failure modes	Failure criteria	Material degradation rules
Fiber tension ( $\sigma_{11} > 0$ )	$R_{ft} = \left( \frac{\sigma_{11}}{X_t^{hyg}} \right)^2 \geq 1$	$E_{11}^d = d_{ft}^{hyg} E_{11}^{hyg}$
Fiber compression ( $\sigma_{11} < 0$ )	$R_{fc} = \left( \frac{\sigma_{11}}{X_c^{hyg}} \right)^2 \geq 1$	$E_{11}^d = d_{fc}^{hyg} E_{11}^{hyg}$
Matrix tension ( $\sigma_{22} > 0$ )	$R_{mt} = \left( \frac{\sigma_{22}}{Y_t^{hyg}} \right)^2 + \left( \frac{\sigma_{12}}{S_{12}^{hyg}} \right)^2 + \left( \frac{\sigma_{23}}{S_{23}^{hyg}} \right)^2 \geq 1$	$E_{22}^d = d_{mt}^{hyg} E_{22}^{hyg}$ , $G_{12}^d = d_{mt}^{hyg} G_{12}^{hyg}$ , $G_{23}^d = d_{mt}^{hyg} G_{23}^{hyg}$ , $v_{12}^d = d_{mt}^{hyg} v_{12}^{hyg}$ , $v_{23}^d = d_{mt}^{hyg} v_{23}^{hyg}$
Matrix compression ( $\sigma_{22} < 0$ )	$R_{mc} = \left( \frac{\sigma_{22}}{Y_c^{hyg}} \right)^2 + \left( \frac{\sigma_{12}}{S_{12}^{hyg}} \right)^2 + \left( \frac{\sigma_{23}}{S_{23}^{hyg}} \right)^2 \geq 1$	$E_{22}^d = d_{mc}^{hyg} E_{22}^{hyg}$ , $G_{12}^d = d_{mc}^{hyg} G_{12}^{hyg}$ , $G_{23}^d = d_{mc}^{hyg} G_{23}^{hyg}$ , $v_{12}^d = d_{mc}^{hyg} v_{12}^{hyg}$ , $v_{23}^d = d_{mc}^{hyg} v_{23}^{hyg}$
Fiber-matrix shear-out ( $\sigma_{11} < 0$ )	$R_{fms} = \left( \frac{\sigma_{11}}{X_c^{hyg}} \right)^2 + \left( \frac{\sigma_{12}}{S_{12}^{hyg}} \right)^2 + \left( \frac{\sigma_{13}}{S_{13}^{hyg}} \right)^2 \geq 1$	$G_{12}^d = d_{fm1}^{hyg} G_{12}^{hyg}$ , $G_{13}^d = d_{fm1}^{hyg} G_{13}^{hyg}$ , $G_{23}^d = d_{fm2}^{hyg} G_{23}^{hyg}$ , $v_{12}^d = d_{fm1}^{hyg} v_{12}^{hyg}$ , $v_{13}^d = d_{fm1}^{hyg} v_{13}^{hyg}$ , $v_{23}^d = d_{fm2}^{hyg} v_{23}^{hyg}$
Interlaminar tension ( $\sigma_{33} > 0$ )	$R_{dt} = \left( \frac{\sigma_{33}}{Z_t^{hyg}} \right)^2 + \left( \frac{\sigma_{13}}{S_{13}^{hyg}} \right)^2 + \left( \frac{\sigma_{23}}{S_{23}^{hyg}} \right)^2 \geq 1$	$E_{33}^d = d_{dt}^{hyg} E_{33}^{hyg}$ , $G_{13}^d = d_{dt}^{hyg} G_{13}^{hyg}$ , $G_{23}^d = d_{dt}^{hyg} G_{23}^{hyg}$ , $v_{13}^d = d_{dt}^{hyg} v_{13}^{hyg}$ , $v_{23}^d = d_{dt}^{hyg} v_{23}^{hyg}$
Interlaminar compression ( $\sigma_{33} < 0$ )	$R_{dc} = \left( \frac{\sigma_{33}}{Z_c^{hyg}} \right)^2 + \left( \frac{\sigma_{13}}{S_{13}^{hyg}} \right)^2 + \left( \frac{\sigma_{23}}{S_{23}^{hyg}} \right)^2 \geq 1$	$E_{33}^d = d_{dc}^{hyg} E_{33}^{hyg}$ , $G_{13}^d = d_{dc}^{hyg} G_{13}^{hyg}$ , $G_{23}^d = d_{dc}^{hyg} G_{23}^{hyg}$ , $v_{13}^d = d_{dc}^{hyg} v_{13}^{hyg}$ , $v_{23}^d = d_{dc}^{hyg} v_{23}^{hyg}$

### 3.2 Elastic-plastic models of metals

In previous studies that analyze the failure of the CFRP-metal bolted joints, the metal material is generally simulated by the elastic model [Ekh, Schön and Zenkert (2013); Riccio and Marciano (2005); Riccio (2005)]. To consider effects of the plastic deformation of the aluminum plate and titanium fastener on failure mechanisms of the hybrid bolted joints, elastic-plastic material models are established in this paper. In order to obtain the elastic-plastic model of the 7050-T7451 aluminum alloy, quasi-static tensile tests of two standard specimens are conducted and the stress-strain curves are depicted in Fig. 3(a). The elastic-plastic model of the Ti-6Al-4V titanium alloy is from Liu et al. [Liu, Zhang, Chen et al. (2015)] and the stress-strain curve is shown in Fig. 3(b). Mechanical properties of the metal materials are listed in Tab. 4.

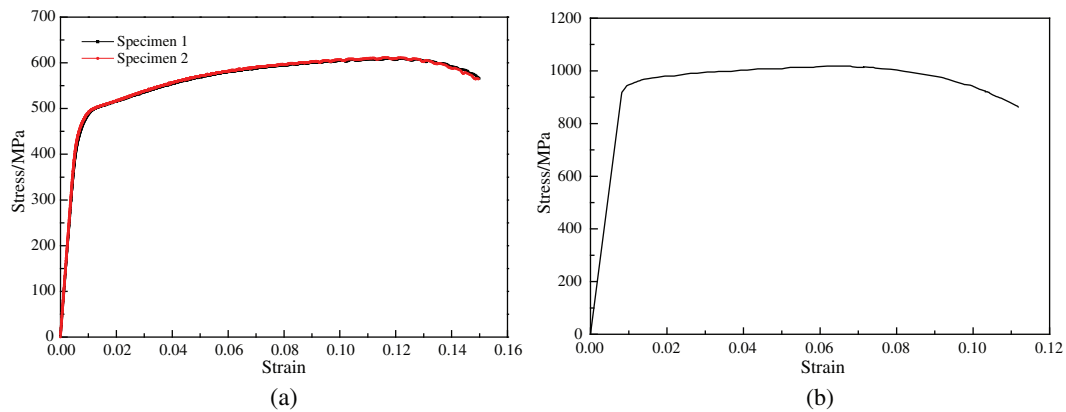


**Figure 3:** Stress-strain curves of the metal materials. (a) 7050-T7451 aluminum alloy (b) Ti-6Al-4V titanium alloy

**Table 4:** Mechanical properties of the metal materials

Items	7050-T7451	Ti-6Al-4V
Elastic modulus $E$ (GPa)	74.5	112
Poisson's ratio $\nu$	0.30	0.34
Elastic limit $\sigma_e$ (MPa)	400	909
Ultimate strength $\sigma_b$ (MPa)	610	1013
Ultimate tensile elongation $\delta$ (%)	15.0	11.2
Thermal expansion coefficient $\alpha$ ( $^{\circ}\text{C}^{-1}$ )	$22.5 \times 10^{-6}$	$9.10 \times 10^{-6}$

### 3.3 Finite element models

As shown in Fig. 4, detailed 3D FE models of the single-lap and double-lap bolted joints were built with the linear hexahedral solid element C3D8 in ABAQUS. A careful mesh

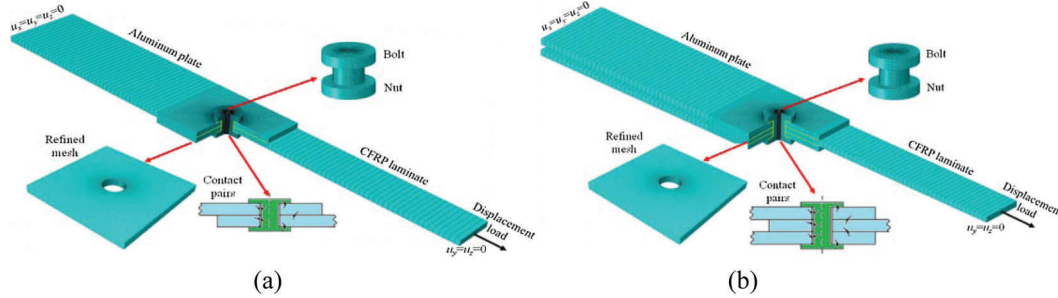


**Figure 4:** FE models of the CFRP-aluminum bolted joints. (a) Single-lap joint (b) Double-lap joint

scheme was designed to obtain accurate stresses of the joints as well as to reduce the computational expense. A refined radial mesh is designed at the overlap section of the joined plates, where the element size of the edges is 1 mm and the element size of the hole is 0.3 mm. Thus, 48 elements and 40 elements are designed along the length and width directions respectively, and 80 elements are around the hole. A relatively coarse mesh is designed at the non-overlap section of the joined plates, where the element size along the length direction is 2.5 mm. Thus, 40 elements are designed along the length and width directions. The element size is 0.74 mm along the thickness direction of the joined plate, which means 4 elements are designed.

Moreover, contact pairs were defined at contact surfaces between the CFRP laminate and aluminum plate, between the CFRP laminate and fastener as well as between the fastener and aluminum plate with the corresponding friction coefficients of 0.2, 0.1, and 0.1. To simulate the experimental loading, three steps were defined. At these steps, the end face of the aluminum plate was constrained in the directions  $x$ ,  $y$  and  $z$  and the end face of the CFRP laminate was constrained in the directions  $y$  and  $z$ . A preload of 1.32 kN was applied to the fastener at the Step 1. A uniform temperature field was applied to the joints at the Step 2 assuming that the temperature was equal at each element of the joints. Finally, a tensile displacement load in the direction  $x$  was imposed on the end face of the CFRP laminate at the Step 3.

To predict the failure of the hybrid bolted joints, a user defined subroutine UMAT that included the PDM of the composites in Section 3.1 was developed and embedded into the FE models. Parameters of the hygrothermal-included PDM of the T800 carbon/epoxy composites are presented in Tab. 5. The parameters of the unified model and the stress analysis model are from Shan et al. [Shan, Zhao, Hong et al. (2018)]. And the degradation factors of the material degradation model are calculated by Eqs. (3) and (4), in which the constituent material parameters are  $V_m=0.424$ ,  $V_f=0.576$ ,  $E_m^0=3.52$  GPa,  $G_m^0=1.30$  GPa,  $j=0.5$  [Hahn (1987); Shan, Zhao, Hong et al. (2018); Zhao, Li, Zhang et al. (2018)]. Besides, elastic and plastic parameters of the metals obtained from the elastic-plastic models in Section 3.2 were input into ABAQUS.

**Table 5:** Parameters of the hygrothermal-included PDM of the T800 carbon/epoxy composites

Parameters of the unified model										
Items	$a$	$b$	$c$	$d$	$e$	$f$	$g$	$h$	$T_g^0/^\circ\text{C}$	$T_g/^\circ\text{C}$
Values	0.04	0.5	0.5	0.04	0.54	0.50	0.50	0.50	185	150
Parameters of the stress analysis model										
Items	$\alpha_{11}$	$\alpha_{22}=\alpha_{33}$	$\alpha_{12}=\alpha_{13}=\alpha_{23}$	$\beta_{11}$	$\beta_{22}=\beta_{33}$	$\beta_{12}=\beta_{13}=\beta_{23}$	$\Delta T/^\circ\text{C}$	$C/\%$		
Values	$-3.16 \times 10^{-6}$	$30.8 \times 10^{-6}$	0	0.008	0.509	0	47	0.62		
Parameters of the material degradation model										
Items	$d_{ft}^0$	$d_{fc}^0$	$d_{mt}^0$	$d_{mc}^0$	$d_{fm1}^0$	$d_{fm2}^0$	$d_{dt}^0$	$d_{dc}^0$		
Values	0.009	0.055	0	0	0.09	0.12	0	0		
Items	$d_{ft}^{hyg}$	$d_{fc}^{hyg}$	$d_{mt}^{hyg}$	$d_{mc}^{hyg}$	$d_{fm1}^{hyg}$	$d_{fm2}^{hyg}$	$d_{dt}^{hyg}$	$d_{dc}^{hyg}$		
Values	0.007	0.040	0	0	0.09	0.12	0	0		

### 3.4 Validations

The proposed numerical model is used to predict the failures of the single-lap and double-lap CFRP-aluminum bolted joints in the RTD and ETW conditions. The numerical load-displacement curves are compared with the experimental curves, as shown in Fig. 5. The predicted curves coincide well with the experimental curves. The predicted ultimate failure loads are also compared with the experimental values in Tab. 6, and the maximum numerical error is less than 5%. Besides, the predicted final failure patterns of the joints are shown in Fig. 6, where the grey region represents the failed area. Large-scale bearing failures of the CFRP laminate are observed in both single-lap and double-lap joints. In

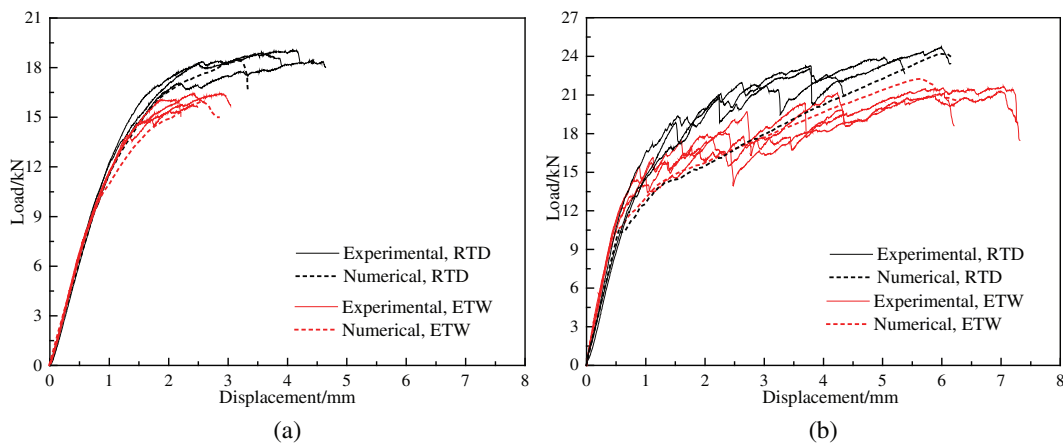


**Figure 5:** Comparisons between numerical and experimental load-displacement curves of the CFRP-aluminum bolted joints. (a) Single-lap joint (b) Double-lap joint

**Table 6:** Experimental and numerical failure loads of the hybrid bolted joints

Type	Condition	Experimental					Numerical	
		$P_{ult}/kN$	$\bar{P}_{ult}/kN$	$S_{n-1}/kN$	COV/%	$\eta$	$P_{ult}/kN$	Error/%
Single-lap joint	RTD	18.40	18.79	0.35	1.9	/	18.43	-1.92
		18.91						
		19.07						
	ETW	16.45	16.15	0.35	2.2	0.86	15.92	-1.42
		16.45						
		15.95						
Double-lap joint	RTD	24.70	23.89	0.83	3.5	/	24.17	1.17
		23.05						
		23.93						
	ETW	21.17	21.33	0.24	1.1	0.89	22.25	4.31
		21.67						
		21.16						
		21.30						

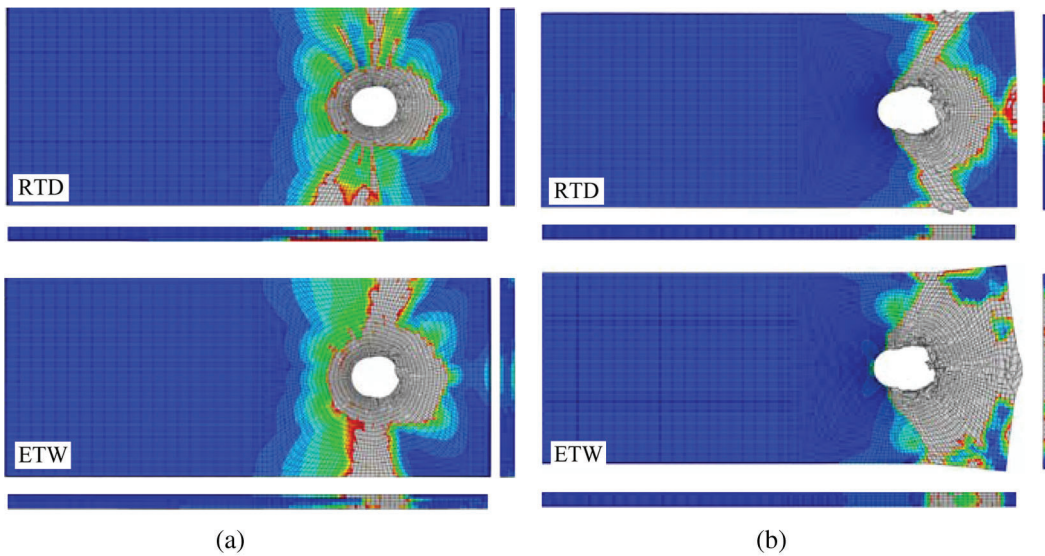


**Figure 6:** Predicted final failure patterns of the CFRP-aluminum bolted joints. (a) Single-lap joint (b) Double-lap joint

the single-lap joint, the bearing failure occurs at both sides of the hole and does not expand to the end of the laminate. In the double-lap joint, the bearing failure occurs at one side of the hole, and expands to the end of the laminate as well as through the wide direction. The predicted failure patterns are consistent with the experimental results (See Fig. 9). Good agreements between the numerical and experimental outcomes suggest that the proposed numerical model can accurately predict the failure of the CFRP-aluminum bolted joints in hygrothermal environments.

#### 4 Hygrothermal effects on failures of the joints based on experiments

##### 4.1 Progressive damage process

The progressive failure processes of the joints in the RTD and ETW conditions are compared based on the experimental load-displacement curves, as shown in Fig. 7. Regarding the single-lap joint in Fig. 7(a), the hygrothermal environment has a negligible influence on the stiffness of the joint at the linear stage (OA), whereas it significantly shortens the progressive damage propagation stage (AB') of the joint. However, concerning the double-lap joint in Fig. 7(b), even though there exists a little difference in the stiffness at the linear stage (OA), the progressive damage propagation processes in the ETW condition (AB') are similar with those in the RTD condition (AB).

Besides, the failure processes of the single-lap and double-lap joints are compared in Fig. 8. Regardless of the environment condition (RTD or ETW), the stiffness of the single-lap joint is much lower than that of the double-lap joint, and the damage of the single-lap joint propagates more rapidly than that of the double-lap joint. However, the hygrothermal environment shortens the progressive damage processes of the single-lap joint more seriously than those of the double-lap joint because of the secondary bending effects of the single-lap joint.

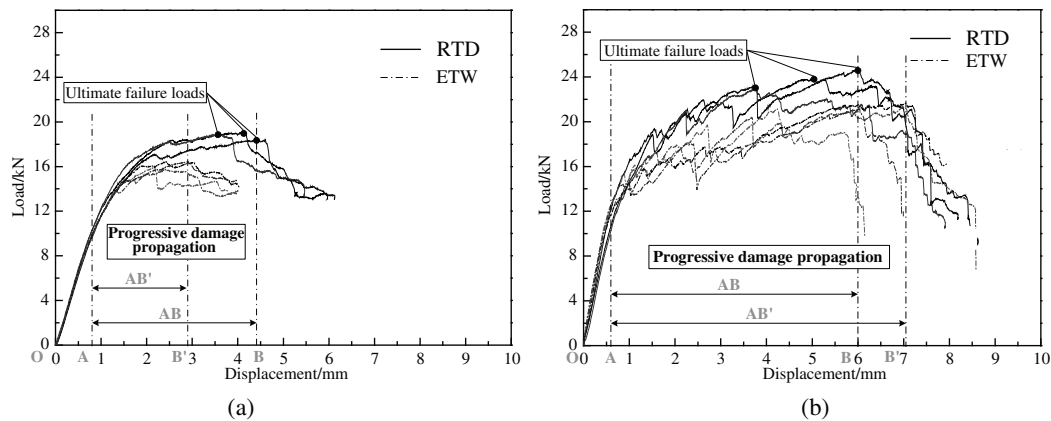


**Figure 7:** Comparisons between progressive failure process of the joints in the RTD and ETW conditions. (a) Single-lap joint (b) Double-lap joint

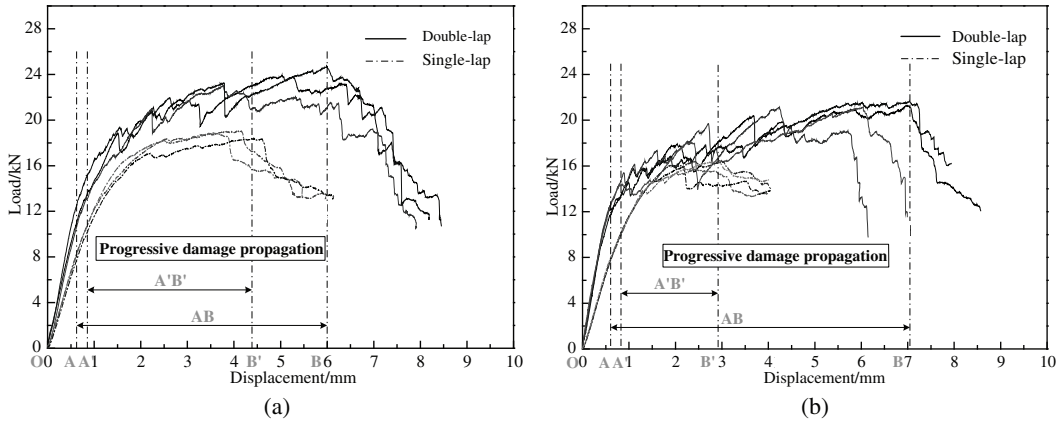


**Figure 8:** Comparisons between progressive failure process of the single-lap and double-lap joints. (a) RTD (b) ETW

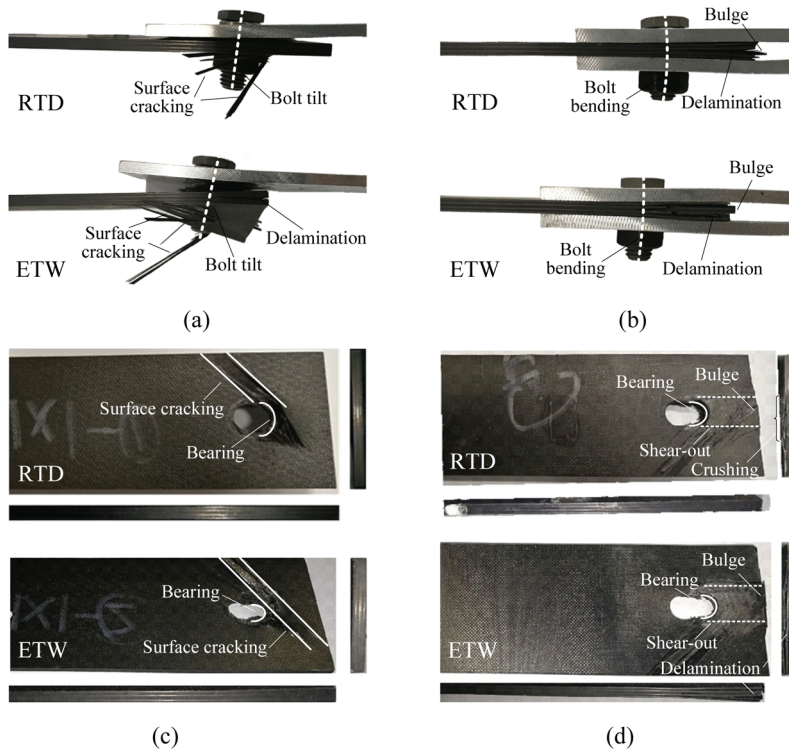


**Figure 9:** Experimental failure patterns of the CFRP-aluminum bolted joints. (a) Single-lap joint. (b) Double-lap joint. (c) CFRP laminate of single-lap joint. (d) CFRP laminate of double-lap joint

#### 4.2 Failure mode

The failure modes of the joints in the RTD and ETW conditions are compared in Fig. 9. Both the collapse failure of the single-lap and double-lap joints in these two conditions is caused by the failure of the CFRP laminate, as depicted in Figs. 9(a) and (b). Considering the single-lap joint in Fig. 9(a), severe bolt tilt and numerous surface cracking occur in both the RTD and ETW conditions, and more serious delamination is introduced in the ETW condition. However, the symmetrical bolt bending accompanied by the delamination and bulge is observed in the double-lap joint in Fig. 9(b). Further, to analyze the damage states of the CFRP laminate, the joints are disassembled, as shown in Figs. 9(c) and (d). As depicted in Fig. 9(c), in both the RTD and ETW conditions, the bearing failure occurs in the CFRP laminate of the single-lap joint. Although the damage region does not extend to the free end of the laminate, the eccentric secondary loading on the single-lap joint aggravates the bearing failure of the CFRP laminate. According to Fig. 9(d), the bearing failure accompanied by the shear-out failure is the leading failure mode of the CFRP laminate of the double-lap joint in the RTD and ETW conditions. The damage region expands along the loading direction and finally reaches the free end of the laminate, which causes the bulge and crushing of the CFRP laminate. To conclude, the CFRP-aluminum single-lap and double-lap bolted joints have different failure mechanisms, and although the hygrothermal environment exacerbates the damage of the CFRP laminate in the joints, it does not change the leading failure mode of the joints.

#### 4.3 Failure load

Tab. 6 presents ultimate failure loads of the single-lap and double-lap joints in the RTD and ETW conditions. To quantitatively evaluate hygrothermal effects on the strength of the joints, a retention  $\eta$  is defined as the ratio of the failure load in the ETW condition to that in the RTD condition. The values of  $\eta$  of the single-lap and double-lap joints are 0.86 and 0.89 respectively, indicating that the hygrothermal environment decreases the failure loads of the CFRP-aluminum bolted joints remarkably. Moreover, the failure loads of the single-lap joint in the RTD and ETW conditions are 21% and 24% less than those of the double-lap joint because of the secondary bending effects. Thus, the joining configuration also considerably affects the failure loads of the hybrid bolted joints.

### 5 Hygrothermal effect analyses based on numerical results

In this section, detailed influence mechanisms of the hygrothermal environment on the tensile failure of the single-lap and double-lap CFRP-aluminum bolted joints were revealed based on the simulation results obtained from the proposed numerical model in Section 3.

#### 5.1 Failure indices around the fastener hole

Because of the anisotropy of the unidirectional composites, a failure index instead of the stress is used to assess the strength margin of the materials around the hole of the CFRP laminate. The failure index is defined as

$$R_{index} = \max(R_{ft}, R_{fc}, R_{mt}, R_{mc}, R_{fms}, R_{dt}, R_{dc}), \quad (5)$$

where  $R_{ft}$ ,  $R_{fc}$ ,  $R_{mt}$ ,  $R_{mc}$ ,  $R_{fms}$ ,  $R_{dt}$  and  $R_{dc}$  are the failure evaluation coefficients in the Hashin-type failure criterion (see Tab. 3). Circular paths are defined at the upper surfaces of each layer of the CFRP laminate, as depicted in Fig. 10. The failure indices along the circular paths under the tensile load 5 kN are extracted from the numerical results, as illustrated in Fig. 11. It can be seen that the distributions of the failure indices of  $45^\circ$ ,  $-45^\circ$ ,  $0^\circ$  and  $90^\circ$  plies are hill-shaped along the circular paths with peak values presented at angles of  $45^\circ$ ,  $-45^\circ$ ,  $0^\circ$  and  $90^\circ$  in sequence. And, the distributions of the failure indices are symmetrical about the middle layer of the CFRP laminate of the double-lap joint, while those of the CFRP laminate of the single-lap joint are asymmetrical due to the secondary bending effects. Besides, the failure indices in the ETW condition are considerably larger than those in the RTD condition, which suggests that the hygrothermal environment reduces the strength margin of the CFRP-aluminum bolted joints before the initial damage occurs.

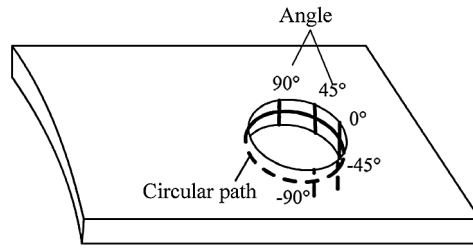
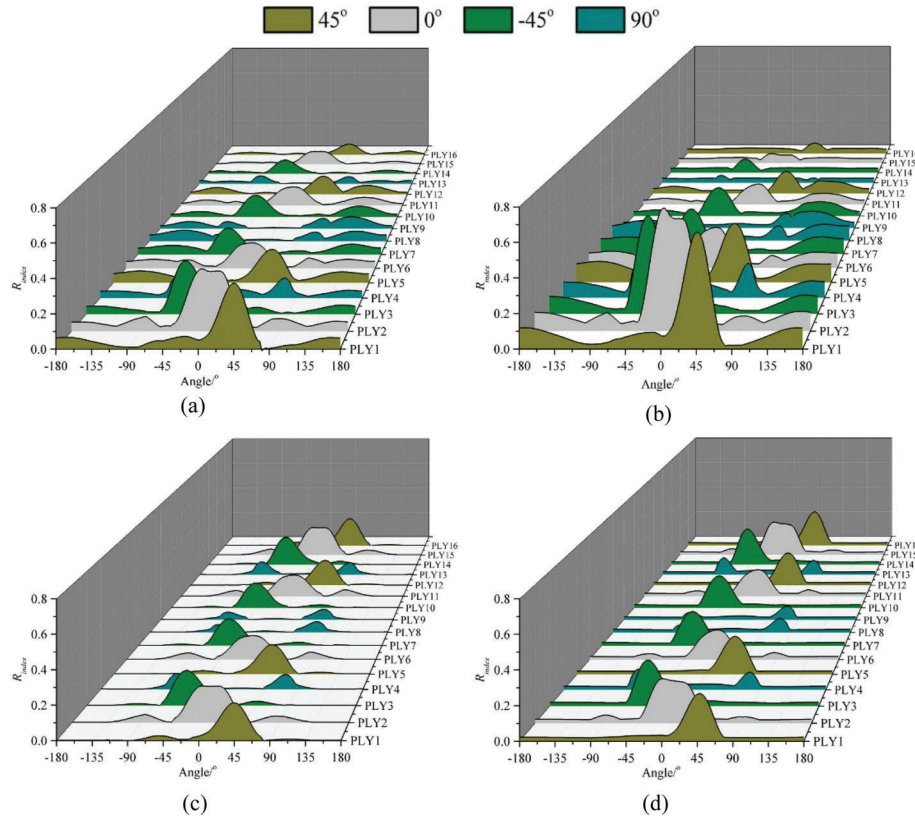


**Figure 10:** Definitions of the circular path and the angle

### 5.2 Contact states between the CFRP and aluminum plates

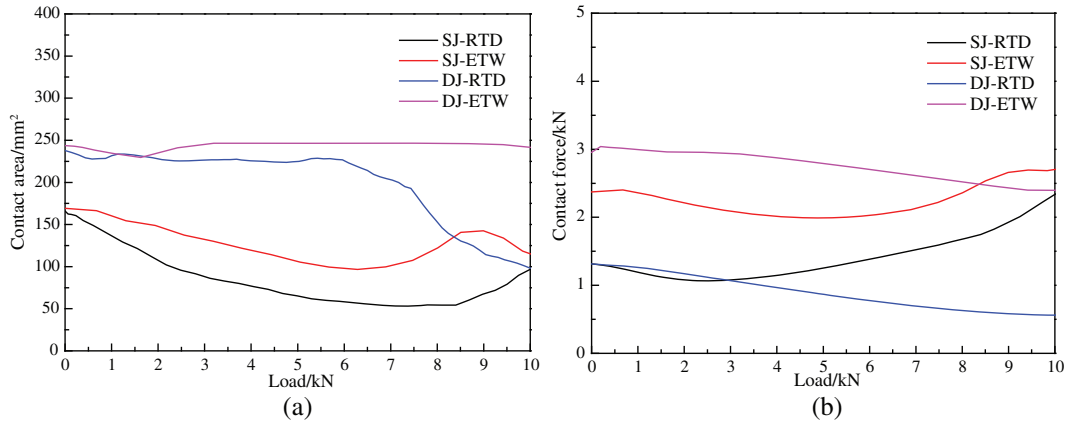
Fig. 12(a) shows how the contact areas between the CFRP laminate and aluminum plate of the single-lap and double-lap joints vary with the increase of the tensile load, in the RTD and ETW conditions. The contact areas in the ETW condition are constantly larger than those in the RTD condition, indicating that the expansion deformations induced by the hygrothermal environment lead to larger contact areas between the joined plates. Moreover, the contact areas between the joined plates of the double-lap joint keep stable at the initial loading stage and then decrease with the increasing tensile load because of the bending of the aluminum plates, while those of the single-lap joint decrease once the tensile load has been applied because the secondary bending effects caused by the eccentric loading results in the departure of the joined plates.

Fig. 12(b) presents how the normal contact forces between the CFRP laminate and aluminum plate of the single-lap and double-lap joints change with the increasing tensile load, in the RTD and ETW conditions. In the RTD condition, the initial normal contact force between the joined plates is 1.32 kN for both the single-lap and double-lap joints, which is resulted from a 2.1 N·m tightening torque. However, in the ETW condition, the



**Figure 11:** Failure indices around the hole of the CFRP laminate in the hybrid bolted joints. (a) Single-lap joint, RTD. (b) Single-lap joint, ETW. (c) Double-lap joint, RTD. (d) Double-lap joint, ETW

normal contact forces between the joined plates of the single-lap and double-lap joints are 2.37 kN and 2.96 kN respectively, which are much larger than the initial preload. It indicates that the interactions among the hygrothermal expansion deformation of the CFRP laminate, the thermal expansion deformation of the aluminum plate, and the thermal expansion deformation of the titanium fastener, enhance the constraint forces along the axis of the bolt. Accordingly, the normal contact force between the CFRP laminate and the aluminum plate is closely related with the tightening force of the bolt, which changes according to the response of the joint when the tensile load is applied because the length of the bolt is kept unchanged. For the single-lap joint, the normal contact force decreases due to the departure of the bolt head from the joined plates caused by the slight tilt of the bolt at the initial stage and then increases with the increasing tensile load because the length of the tilted bolt is smaller than the total thickness of the joined plates, which causes remarkable pressure on the joined plates. Regarding the double-lap joint, the



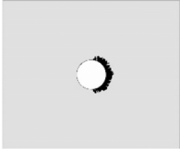
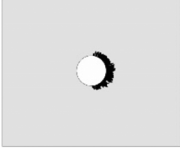
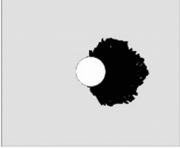
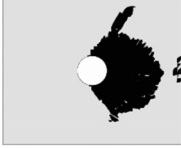
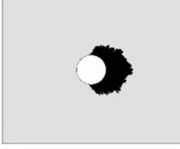
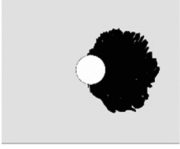
**Figure 12:** Variations of contact area and normal contact force between the CFRP and aluminum plates of the hybrid bolted joints. (a) Contact area vs. tensile load. (b) Normal contact force vs. tensile load

contact force decreased slowly with the increasing tensile load because the bending of the bolt reduces the contact area between the bolt head and joined plates, which further leads to the decrease of the normal contact force.

### 5.3 Damage propagation processes

In order to compare the damage propagation processes of the joints in the RTD and ETW conditions, the damage patterns of the single-lap and double-lap joints at three representative states (State A: the end of the linear stage; State B: the middle of the damage propagation; State C: the ultimate failure) are illustrated in Tab. 7. Regarding the single-lap joint, the damage initiates at the bearing side of the hole and then remarkably enlarges around the hole of the joint, which is caused by the inclined bolt. Although the damage area is small and does not extend to the edge of the laminate, the tensile load cannot be transferred between the bolt and the laminate of the single-lap joint. Similarly, the damage of the double-lap joint also begins at the bearing side of the hole. However, the damage area concentrates at the bearing side of the hole, markedly enlarges along the loading direction and finally reaches the end of the laminate. The tensile load can be transferred between the bolt and the laminate during this long damage propagation process. Therefore, the double-lap joint can transfer the load more efficiently than the single-lap joint. Compared with the damage states of the single-lap and double-lap joints in the RTD condition, more severe damage is found for the joints in the ETW condition, indicating that the hygrothermal environment aggravates the damage extent of the single-lap and the double-lap joints.

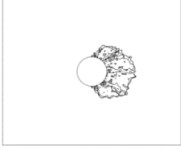
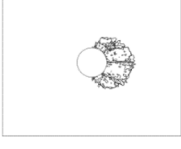
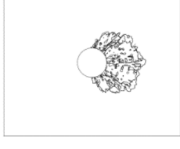
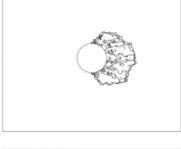
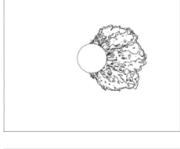
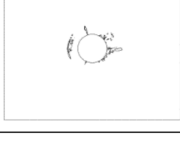
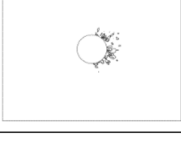
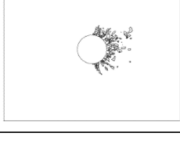
**Table 7:** Damage propagation processes of the CFRP laminate in the hybrid bolted joints

Condition	State A	State B	State C
Single-lap joint, RTD			
Single-lap joint, ETW			
Double-lap joint, RTD			
Double-lap joint, ETW			

#### 5.4 Microscopic failure modes

Tab. 8 shows the seven microscopic failure modes of the CFRP laminate under the tensile load 15 kN to compare the extent of microscopic damage of the single-lap and double-lap joints, in the RTD and ETW conditions. Generally, the seven microscopic failures occur around the bearing side of the hole and extend along the loading direction in the single-lap and double-lap joints, while extra failures around the other side of the hole are induced in the single-lap joint because of the significantly tilted bolt. And the single-lap and double-lap joints in the ETW condition have much larger failure areas than those in the RTD condition. In detail, negligible fiber tension failures and slight matrix tension failures are observed in both the RTD and ETW conditions. In contrast, fiber and matrix compression failures are severe in these two conditions. As for the interlaminar failures, interlaminar tension failures are much more serious than interlaminar compression failures in both conditions. Consequently, the fiber compression failure, the matrix compression failure, the fiber-matrix shear-out failure, and the interlaminar tension failure

**Table 8:** Microscopic failure modes of the CFRP laminate in the hybrid bolted joints

Condition	Single-lap joint, RTD	Single-lap joint, ETW	Double-lap joint, RTD	Double-lap joint, ETW
Fiber tension				
Fiber compression				
Matrix tension				
Matrix compression				
Fiber-matrix shear-out				
Interlaminar tension				
Interlaminar compression				

of the CFRP laminate are the leading microscopic failure modes that cause the final failure of the CFRP-aluminum bolted joints. And the hygrothermal environment accelerates the microscopic failures of the CFRP laminate, and further weakens the strength of the joints.

## 6 Conclusions

Influences of the hygrothermal environment on tensile failures of the single-lap and double-lap CFRP-aluminum bolted joints were thoroughly investigated by combining experiments with a novel numerical model. In the proposed failure prediction model, a hygrothermal-included progressive damage model of composites was established, and elastic-plastic models of metals were built. Good consistency between the numerical and experimental outcomes suggested the effectiveness of the proposed scheme in predicting the failure of the hybrid bolted joints in hygrothermal environments. Further, different failure mechanisms of the single-lap and double-lap bolted joints in the RTD and ETW conditions were revealed, respectively. It concludes that both the collapse failures of the single-lap and double-lap bolted joints in these two conditions were dominated by the bearing failure of the CFRP hole laminate, which showed that the hygrothermal environment did not change the macro failure modes of the joints. However, the hygrothermal environment considerably shortened the damage propagation processes, and decreased the strength of the single-lap and double-lap bolted joints by 14% and 11%, respectively. Besides, in both the RTD and ETW conditions, the load-transfer capability of the single-lap joint was inferior to that of the double-lap joint because of the secondary bending effects. And the hygrothermal environment weakened the strength of the single-lap joint more severely than the double-lap joint, because it obviously aggravated the secondary bending effects of the single-lap joint.

**Acknowledgement:** This work is supported by the National Science Foundation of China (11772028, 11872131, 11702012, U1864208, 11572058 and 11372020) and the Academic Excellence Foundation of BUAA for PhD Students.

**Funding Statement:** The author(s) received no specific funding for this study.

**Conflicts of Interest:** The authors declare that they have no conflicts of interest to report regarding the present study.

## References

- Abdus, S.; Cheng, X.; Huang, W.; Ahmed, A.; Hu, R.** (2019): Bearing failure and influence factors analysis of metal-to-composite bolted joints at high temperature. *Journal of the Brazilian Society of Mechanical Sciences and Engineering*, vol. 41, no. 298, pp. 1-11. DOI 10.1007/s40430-019-1797-5.
- Ahmad, H.; Crocombe, A. D.; Smith, P. A.** (2013): Strength prediction in CFRP woven laminate bolted double-lap joints under quasi-static loading using XFEM. *Composites Part A*, vol. 56, pp. 192-202. DOI 10.1016/j.compositesa.2013.10.012.

**Ahmad, H.; Crocombe, A. D.; Smith, P. A.** (2014): Strength prediction in CFRP woven laminate bolted single-lap joints under quasi-static loading using XFEM. *Composites Part A*, vol. 66, pp. 82-93. DOI 10.1016/j.compositesa.2014.07.013.

**Askri, R.; Bois, C.; Wagnier, H.; Gayton, N.** (2018): Tolerance synthesis of fastened metal-composite joints based on probabilistic and worst-case approaches. *Computer-Aided Design*, vol. 100, pp. 39-51. DOI 10.1016/j.cad.2018.02.008.

**ASTM D5229M-14.** (2014). Standard test method for moisture absorption properties and equilibrium conditioning of polymer matrix composite materials. *American Society for Testing of Material*.

**ASTM D5961M-13.** (2013). Standard test method for bearing response of polymer matrix composite laminates. *American Society for Testing of Material*.

**Banea, M. D.; Rosioara, M.; Carbas, R. J. C.; Silva, L. F. M.** (2018): Multi-material adhesive joints for automotive industry. *Composites Part B*, vol. 151, pp. 71-77. DOI 10.1016/j.compositesb.2018.06.009.

**Caccese, V.; Berube, K. A.; Fernandez, M.; Melo, J. D.; Kabche, J. P.** (2009): Influence of stress relaxation on clamp-up force in hybrid composite-to-metal bolted joints. *Composite Structures*, vol. 89, no. 2, pp. 285-293. DOI 10.1016/j.compstruct.2008.07.031.

**Camanho, P. P.; Matthews, F. L.** (1997): Stress analysis and strength prediction of mechanically fastened joints in FRP-a review. *Composites Part A*, vol. 28A, no. 6, pp. 529-547. DOI 10.1016/S1359-835X(97)00004-3.

**Coelho, A. M. G.; Mottram, J. T.** (2015): A review of the behaviour and analysis of bolted connections and joints in pultruded fibre reinforced polymers. *Materials and Design*, vol. 74, pp. 86-107. DOI 10.1016/j.matdes.2015.02.011.

**Coman, C. D.; Constantinescu, D. M.** (2019): Temperature effects on joint strength and failure modes of hybrid aluminum-composite countersunk bolted joints. *Proceedings of the Institution of Mechanical Engineers, Part L: Journal of Materials: Design and Applications*, vol. 233, no. 11, pp. 2204-2218. DOI 10.1177/1464420719837299.

**Comer, A. J.; Dhôte, J. X.; Stanley, W. F.; Young, T. M.** (2012): Thermo-mechanical fatigue analysis of liquid shim in mechanically fastened hybrid joints for aerospace applications. *Composite Structures*, vol. 94, no. 7, pp. 2181-2187. DOI 10.1016/j.compstruct.2012.01.008.

**Egan, B.; McCarthy, C. T.; McCarthy, M. A.; Gray, P. J.; O'Higgins, R. M.** (2013): Static and high-rate loading of single and multi-bolt carbon-epoxy aircraft fuselage joints. *Composites Part A*, vol. 53, pp. 97-108. DOI 10.1016/j.compositesa.2013.05.006.

**Ekh, J.; Schön, J.; Melin, L. G.** (2006): Load transfer in multirow, single shear, composite-to-aluminum lap joints. *Composite Science and Technology*, vol. 66, no. 7-8, pp. 875-885. DOI 10.1016/j.compscitech.2005.08.015.

**Ekh, J.; Schön, J.; Melin, L. G.** (2005): Secondary bending in multi fastener, composite-to-aluminium single shear lap joints. *Composites Part B*, vol. 36, no. 3, pp. 195-208. DOI 10.1016/j.compositesb.2004.09.001.

**Ekh, J.; Schön, J.; Zenkert, D.** (2013): Simple and efficient prediction of bearing failure in single shear, composite lap joints. *Composite Structures*, vol. 105, pp. 35-44. DOI 10.1016/j.compstruct.2013.04.038.

**Ekh, J.; Schön, J.** (2008): Finite element modeling and optimization of load transfer in multi-fastener joints using structural elements. *Composite Structures*, vol. 82, no. 2, pp. 245-256. DOI 10.1016/j.compstruct.2007.01.005.

**Gay, A.; Lefebvre, F.; Bergamo, S.; Valiorgue, F.; Chalandon, P. et al.** (2016): Fatigue performance of a self-piercing rivet joint between aluminum and glass fiber reinforced thermoplastic composite. *International Journal of Fatigue*, vol. 83, pp. 127-134. DOI 10.1016/j.ijfatigue.2015.10.004.

**Giannopoulos, I. K.; Dawes, D. D.; Kourousis, K. I.; Yasaee, M.** (2017): Effects of bolt torque tightening on the strength and fatigue life of airframe FRP laminate bolted joints. *Composites Part B*, vol. 125, pp. 19-26. DOI 10.1016/j.compositesb.2017.05.059.

**Graham, D. P.; Rezai, A.; Baker, D.; Smith, P. A.; Watts, J. F.** (2014): The development and scalability of a high strength, damage tolerant, hybrid joining scheme for composite-metal structures. *Composites Part A*, vol. 64, pp. 11-24. DOI 10.1016/j.compositesa.2014.04.018.

**Hahn, H. T.** (1987): Hygrothermal damage in graphite/epoxy laminates. *Journal of Engineering Materials and Technology*, vol. 109, no. 1, pp. 3-11. DOI 10.1115/1.3225930.

**Horn, W. J.; Schmitt, R. R.** (1993). Relaxation in bolted thermoplastic composite joints. *AIAA/ASME/ASCE/AHS/ASC 34th Structures, Structural Dynamics, and Materials Conference, La Jolla, CA, USA*, pp. 485-494.

**Jiang, H.; Li, G.; Zhang, X.; Cui, J.** (2017): Fatigue and failure mechanism in carbon fiber reinforced plastics/aluminum alloy single lap joint produced by electromagnetic riveting technique. *Composite Science and Technology*, vol. 152, pp. 1-10. DOI 10.1016/j.compscitech.2017.09.004.

**Kapidzic, Z.; Ansell, H.; Schön, J.; Simonsson, K.** (2015a): Fatigue bearing failure of CFRP composite in biaxially loaded bolted joints at elevated temperature. *Composite Structures*, vol. 127, pp. 298-307.

**Kapidzic, Z.; Ansell, H.; Schön, J.; Simonsson, K.** (2015b): Quasi-static bearing failure of CFRP composite in biaxially loaded bolted joints. *Composite Structures*, vol. 125, pp. 60-71.

**Kapidzic, Z.; Ansell, H.; Schön, J.; Simonsson, K.** (2016): Fatigue bearing failure of CFRP composite in bolted joints exposed to biaxial variable amplitude loading at elevated temperature. *Composite Structures*, vol. 142, pp. 71-77. DOI 10.1016/j.compstruct.2016.01.064.

**Kapidzic, Z.; Nilsson, L.; Ansell, H.** (2014): Finite element modeling of mechanically fastened composite-aluminum joints in aircraft structures. *Composite Structures*, vol. 109, pp. 198-210. DOI 10.1016/j.compstruct.2013.10.056.

**Kradinov, V.; Barut, A.; Madenci, E.; Ambur, D. R.** (2001): Bolted double-lap composite joints under mechanical and thermal loading. *International Journal of Solids and Structures*, vol. 38, no. 44-45, pp. 7801-7837. DOI 10.1016/S0020-7683(01)00128-7.

- Li, H.; Zhang, K.; Cheng, H.; Suo, H.; Cheng, Y. et al.** (2019): Multi-stage mechanical behavior and failure mechanism analysis of CFRP/Al single-lap bolted joints with different seawater ageing conditions. *Composite Structures*, vol. 208, pp. 634-645. DOI 10.1016/j.compstruct.2018.10.044.
- Li, H. S.; Gu, R. J.; Zhao, X.** (2017): Global sensitivity analysis of load distribution and displacement in multi-bolt composite joints. *Composites Part B*, vol. 116, pp. 200-210. DOI 10.1016/j.compositesb.2017.01.058.
- Liu, F.; Lu, X.; Zhao, L.; Zhang, J.; Hu, N. et al.** (2018): An interpretation of the load distributions in highly torqued single-lap composite bolted joints with bolt-hole clearances. *Composites Part B*, vol. 138, pp. 194-205. DOI 10.1016/j.compositesb.2017.11.027.
- Liu, L.; Zhang, J.; Chen, K.; Wang, H.; Liu, M.** (2015): Experimental and numerical analysis of the mechanical behavior of composite-to-titanium bolted joints with liquid shim. *Aerospace Science and Technology*, vol. 49, no. 5, pp. 167-172. DOI 10.1016/j.ast.2015.11.029.
- Liu, L.** (2014): The influence of the substrate's stiffness on the liquid shim effect in composite-to-titanium hybrid bolted joints. *Proceedings of the Institution of Mechanical Engineers, Part G: Journal of Aerospace Engineering*, vol. 228, no. 3, pp. 470-479. DOI 10.1177/0954410013476612.
- Mangalgi, P. D.** (2013): Design allowable considerations for use of laminated composites in aircraft structures. *Journal of the Indian Institute of Science*, vol. 93, no. 4, pp. 571-592.
- McCarthy, M. A.** (2001): BOJCAS: bolted joints in composite aircraft structures. *Air & Space Europe*, vol. 3, no. 3/4, pp. 139-142. DOI 10.1016/S1290-0958(01)90077-2.
- Meram, A.; Can, A.** (2019): Experimental investigation of screwed joints capabilities for the CFRP composite laminates. *Composites Part B: Engineering*, vol. 176, pp. 107142. DOI 10.1016/j.compositesb.2019.107142.
- Naarayan, S. S.; Kumar, D. V. T. G. P.; Chandra, S.** (2009): Implication of unequal rivet load distribution in the failures and damage tolerant design of metal and composite civil aircraft riveted lap joints. *Engineering Failure Analysis*, vol. 16, no. 7, pp. 2255-2273. DOI 10.1016/j.engfailanal.2009.03.016.
- Nichols, J. M.; Trickey, S. T.; Seaver, M.; Motley, S. R.; Eisner, E. D.** (2007): Using ambient vibrations to detect loosening of a composite-to-metal bolted joint in the presence of strong temperature fluctuations. *Transactions of the ASME*, vol. 129, pp. 710-717.
- Pitta, S.; Carles, V. M.; Roure, F.; Crespo, D.; Rojas, J. I.** (2018): On the static strength of aluminium and carbon fibre aircraft lap joint repairs. *Composite Structures*, vol. 201, pp. 276-290. DOI 10.1016/j.compstruct.2018.06.002.
- Pramanik, A.; Basak, A. K.; Dong, Y.; Sarker, P. K.; Uddin, M. S. et al.** (2017): Joining of carbon fibre reinforced polymer (CFRP) composites and aluminium alloys-a review. *Composites Part A*, vol. 101, pp. 1-29. DOI 10.1016/j.compositesa.2017.06.007.

- Rao, H. M.; Kang, J.; Huff, G.; Avery, K.** (2018): Impact of specimen configuration on fatigue properties of self-piercing riveted aluminum to carbon fiber reinforced polymer composite. *International Journal of Fatigue*, vol. 113, pp. 11-22. DOI 10.1016/j.ijfatigue.2018.03.031.
- Riccio, A.; Marciano, L.** (2005): Effects of geometrical and material features on damage onset and propagation in single-lap bolted composite joints under tensile load: part I-experimental studies. *Journal of Composite Materials*, vol. 39, no. 23, pp. 2071-2090. DOI 10.1177/0021998305052026.
- Riccio, A.** (2005): Effects of geometrical and material features on damage onset and propagation in single-lap bolted composite joints under tensile load: part II-numerical studies. *Journal of Composite Materials*, vol. 39, no. 23, pp. 2091-2112. DOI 10.1177/0021998305052027.
- Shan, M.; Zhao, L.; Hong, H.; Liu, F.; Zhang, J.** (2018): A progressive fatigue damage model for composite structures in hygrothermal environments. *International Journal of Fatigue*, vol. 111, pp. 299-307. DOI 10.1016/j.ijfatigue.2018.02.019.
- Tajeuna, T. A. D.; Légeron, F.; Labossière, P.; Demers, M.; Langlois, S.** (2015): Effect of geometrical parameters of aluminum-to-steel bolted connections. *Engineering Structures*, vol. 102, pp. 344-357. DOI 10.1016/j.engstruct.2015.08.010.
- Tang, H.; Liu, L.** (2018): A novel metal-composite joint and its structural performance. *Composite Structures*, vol. 206, pp. 33-41. DOI 10.1016/j.compstruct.2018.07.111.
- Thoppul, S. D.; Finegan, J.; Gibson, R. F.** (2009): Mechanics of mechanically fastened joints in polymer-matrix composite structures-a review. *Composite Science and Technology*, vol. 69, no. 3-4, pp. 301-329. DOI 10.1016/j.compscitech.2008.09.037.
- Tian, B. J.; Xiong, J. J.; Liu, J. Z.** (2015): A new approach for evaluating fatigue lives of multi-fastener mechanical joints based on a nominal stress concept and minimal datasets. *International Journal of Fatigue*, vol. 80, pp. 257-265. DOI 10.1016/j.ijfatigue.2015.06.013.
- Tserpes, K. I.; Labeas, G.; Papanikos, P.; Kermanidis, T.** (2002): Strength prediction of bolted joints in graphite/epoxy composite laminates. *Composites Part B*, vol. 33, no. 7, pp. 521-529. DOI 10.1016/S1359-8368(02)00033-1.
- Tüzemen, M.; Salame, E.; Avc, A.** (2017): Enhancing mechanical properties of bolted carbon/epoxy nanocomposites with carbon nanotube, nanoclay, and hybrid loading. *Composites Part B*, vol. 128, pp. 146-154. DOI 10.1016/j.compositesb.2017.07.001.
- VanderKlok, A.; Dutta, A.; Tekalur, S. A.** (2013): Metal to composite bolted joint behavior evaluated at impact rates of loading. *Composite Structures*, vol. 106, pp. 446-452. DOI 10.1016/j.compstruct.2013.06.004.
- Yang, B.; Yue, Z.; Geng, X.; Guan, X.; Wang, P.** (2017): Experimental and numerical study on bearing failure of countersunk composite-composite and composite-steel joint. *Journal of Composite Materials*, vol. 51, no. 22, pp. 3211-3224. DOI 10.1177/0021998316684936.

**Zhang, D.; Zhang, Q.; Fan, X.; Zhao, S.** (2019): Review on joining process of carbon fiber-reinforced polymer and metal: applications and outlook. *Rare Metal Materials and Engineering*, vol. 48, no. 1, pp. 44-54.

**Zhang, J.; Zhou, L.; Chen, Y.; Zhao, L.; Fei, B.** (2016): A micromechanics-based degradation model for composite progressive damage analysis. *Journal of Composite Materials*, vol. 50, no. 16, pp. 2271-2287. DOI 10.1177/0021998315602947.

**Zhao, L.; Li, Y.; Zhang, J.; Zhou, L.; Hu, N.** (2018): A novel material degradation model for unidirectional CFRP composites. *Composites Part B*, vol. 135, pp. 84-94. DOI 10.1016/j.compositesb.2017.09.038.

**Zhao, L.; Shan, M.; Liu, F.; Zhang, J.** (2017): A probabilistic model for strength analysis of composite double-lap single-bolt joints. *Composite Structures*, vol. 161, pp. 419-427. DOI 10.1016/j.compstruct.2016.11.074.

**Zuo, Y.; Cao, Z.; Cao, Y.; Zhang, Q.; Wang, W.** (2018): Dynamic behavior of CFRP-Ti single-lap pinned joints under longitudinal electromagnetic dynamic loading. *Composite Structures*, vol. 184, pp. 362-371. DOI 10.1016/j.compstruct.2017.09.079.